




Visible light-driven photocatalyst δ -Bi₇VO₁₃ nanoparticles synthesized by thermal plasma

Shankar S. Kekade^{1,2,*} , Suyog A. Raut^{2,4}, Ram J. Choudhary³, Trupti S. Barve⁵, Vikas L. Mathe², Deodatta M. Phase³, Damien Thiry⁴, and Shankar I. Patil²

¹ Department of Physics, Radhabai Kale Mahila Mahavidyalaya, Ahemdnagar 414001, India

² Department of Physics, Savitribai Phule Pune University, Ganeshkhind, Pune 411007, India

³ Consortium for Scientific Research, UGC-DAE, Khandwa Road, Indore 452001, India

⁴ Chimie des Interactions Plasma Surfaces (ChIPS), University of Mons, 7000 Mons, Belgium

⁵ Department of Zoology, New Arts Commerce & Science College, Ahmednagar 414001, India

Received: 9 September 2023

Accepted: 23 November 2023

© The Author(s), under exclusive licence to Springer Science+Business Media, LLC, part of Springer Nature, 2023

ABSTRACT

Understanding the electronic structure of photocatalysts is crucial for enhancing their efficiency. In this study, we have successfully synthesized novel monoclinic bismuth vanadate (Bi₇VO₁₃) nanoparticles using the gas phase condensation technique, with an average particle size of 40 nm. To investigate the crystallographic structure of the as-synthesized nanoparticles, we conducted X-ray diffraction (XRD) experiments. Additionally, we employed advanced characterization techniques to provide a detailed analysis of the electronic structure of Bi₇VO₁₃ nanoparticles. This study presents the first report on the electronic structure of Bi₇VO₁₃ nanoparticles using the aforementioned spectroscopic methods. Remarkably, the investigation revealed that the valence band maximum (VB) and conduction band minimum (CB) are dominated by O 2p and V 3d states, respectively.

Moreover, X-ray absorption spectroscopy (XAS) reveals splitting the V 3d conduction band state into a triplet d-manifold at the V L-edge and O K-edge. This splitting arises from the lattice distortion induced by lone pairs, which gives rise to a band gap of 2.28 eV. Under visible light irradiation, the Bi₇VO₁₃ nanoparticles exhibit efficient visible light absorption, highlighting their potential for photocatalytic applications. Notably, our experiments demonstrated outstanding photodegradation properties of methylene blue, serving as a model effluent, further underscoring the photocatalytic progress of Bi₇VO₁₃ nanoparticles. In conclusion, this research explains the functioning of Bi₇VO₁₃ photocatalysts and opens the doors for utilizing their potential to generate a cleaner and brighter future.

Address correspondence to E-mail: shankarkekade@gmail.com

1 Introduction

Semiconductor nanomaterials have gained significant attention for their potential applications in hydrogen production, energy harvesting, global environmental pollutant control, and the degradation of organic compounds. In our everyday lives, water pollution has emerged as a prominent issue, mainly stemming from the use of harmful chemical compounds. Photocatalysis utilizing solar light presents an ideal technology for environmental remediation and sustainable wastewater management. Currently, researchers are facing the challenge of efficiently degrading wastewater containing harmful organic molecules, posing a threat to the environment. Wastewater, often released untreated into rivers, poses a severe problem to water ecosystems due to hazardous dyes, pesticides, endocrine disruptors, and other harmful substances. Addressing the degradation of such wastewater containing organic molecules remains a significant challenge for researchers [1]. Concerning energy and environmental matters, the semiconductor photocatalyst has gained considerable interest due to its potential applications in hydrogen production, the breakdown of organic compounds, and the regulation of global environmental pollutants [2, 3]. Many semiconductor photocatalysts have been explored by considering their physical and chemical properties. TiO_2 , ZnO , and many semiconductor photocatalysts are only excited by ultraviolet irradiation, less than 5% of the sunlight [4]. An urgent need is to develop a photocatalyst capable of harnessing visible light emission from the solar spectrum for efficient utilization. However, many researchers have made significant efforts to develop a visible light photocatalyst using metal oxide semiconductors such as Fe_2O_3 [5], WO_3 [6], Bi_2O_3 [7], BiVO_4 [8], Bi_2WO_6 [9], and $\text{Bi}_{11}\text{VO}_{19}$ [10].

Due to its structural diversity and attractive physical properties, such as a narrow band gap (2.3–2.9 eV), the ability to absorb visible light, high chemical stability, and low toxicity, bismuth vanadate emerges as a compelling choice for photocatalysis and water splitting applications [11, 12]. The bismuth vanadate exhibits hybridization between the Bi 6s and O 2p energy levels, observed in the valence band's upper region. This hybridization is particularly evident in the fluorite-type structure of bismuth vanadate, where the Bi^{3+} ion possesses a high degree of polarizability due to its lone pair of electrons. The presence of the Bi^{3+} cation with a lone pair leads to

enhanced ionic conductivity, potentially due to the formation of weak Bi–O bonds. This characteristic contributes to a small band gap and high hole mobility [13, 14]. In the earlier study in photocatalysis, a bismuth compound was used to modify TiO_2 . In the various Bi-based compounds, such as Bi_2O_3 [15], BiOX (Cl, Br, I), [16–18], Bi_2WO_6 [19], Bi_2MoO_6 [20], $\text{Bi}_{11}\text{VO}_{19}$ [14] and excellent photocatalytic properties have been found. Due to the high recombination rate of the photogenerated electron-hole pairs and the boundedness of the visible light response region, there were still some limitations on using the Bi-based compound for photocatalysis. There is a need to address this limitation to search for some Bi-based compounds and to study the electronic structure, band gap, and band potential of Bi-based compounds to enhance the photocatalytic activity.

Their nano size demonstrates the efficient photocatalytic activity of bismuth vanadates in various forms, such as nanoparticles, nanotubes, nanowires, nanosheets, and nanorods. Different synthesis methods, including hydrothermal, co-precipitation, and sol-gel, hydrothermal, co-precipitation, and sol-gel, are employed to produce nano-sized forms of bismuth vanadate. While non-plasma methods offer advantages such as the possibility of oriented growth and growth on large patterned substrates, these synthesis methods may compromise purity due to the use of catalysts. The sol-gel method is widely employed and well known for its narrow size distribution, small particle size and high yield, but it still exhibits variations in chemical reactions depending on the material. However, this method may compromise purity and require significant time and post-synthesis treatments [21]. Nanoparticle synthesis can be achieved using the thermal plasma method, a high-temperature technique. It offers several advantages, including high rates of chemical reactions, production of high-purity products, no requirement for high vacuum conditions, shorter synthesis time, and formation of highly crystalline products. In order to control the growth of nanoparticles in the thermal plasma method, various parameters need to be controlled. In this study, we synthesized the high-temperature phase of $\text{Bi}_7\text{VO}_{13}$ using the thermal plasma method.

The primary objective of this article is to demonstrate the synthesis, electronic properties, and photocatalytic activity of $\text{Bi}_7\text{VO}_{13}$ nanoparticles synthesized via the thermal plasma method. The bismuth vanadate nanoparticles exhibit promising potential for the

photodegradation of methylene blue (MB) under visible light irradiation.

2 Experiment

2.1 Materials and methods

To prepare $\text{Bi}_7\text{VO}_{13}$ nanoparticles, the precursors are bismuth oxide (Bi_2O_3), vanadium pentoxide (V_2O_5), and graphite powder. All these synthesis precursors were purchased from Sigma Aldrich with 99.9% purity and used as received without further purification.

2.2 Method of synthesis

In this study, the synthesis of $\text{Bi}_7\text{VO}_{13}$ nanoparticles was conducted through a homogeneous gas phase condensation process utilizing a direct current transferred arc thermal plasma reactor (DCTATPR). To prepare the nanoparticles, precursor pellets containing Bi_2O_3 and V_2O_5 oxide powders were mixed in a 1:1 atomic ratio with graphite powder to enhance conductivity. The mixture was then pelletized using a 100 kg/cm^2 pressure hydraulic press. The resulting pellets were positioned on a water-cooled graphite anode. [14, 22]. The experimental operating parameters are shown in Table 1.

2.3 Characterization

The crystal structure of the $\text{Bi}_7\text{VO}_{13}$ nanoparticles was investigated using the X-ray diffraction (XRD) technique using Bruker AXS D8 advance X-ray diffractometer equipped with $\text{Cu K}\alpha$ radiations ($\lambda = 1.54 \text{ \AA}$).

Table 1 Typical synthesis parameters of DCTATPR for $\text{Bi}_7\text{VO}_{13}$ nanoparticles

Sr. No	Physical parameters	Operating parameters
1	DC power (kW)	6 (kW)
2	Arc length	50-60 mm
3	Gas flow rates (LPM)	6 + 5
	Plasma-forming gas	4 + 4
	(Argon + Nitrogen)	
	Ambient gas	
	(Argon) + Oxygen	
4	Base pressure	10^{-3} (Torr)
5	Operating pressure	250 (Torr)

Raman spectroscopy measurement was performed with a Raman spectrometer (Renishaw InVia micro-Raman spectrometer) using a He–Ne laser with a wavelength of 532 nm. The Transmission Electron Microscopy (TEM) images, Selected Area Electron Diffraction (SAED) patterns, and elemental mapping with Scanning Transmission Electron Microscopy (STEM) mode are performed by the High Resolution-Transmission Electron Microscopy (HR-TEM) technique (Tecnai G2 S-TWIN). The UV–visible diffuse reflectance spectra (DRS) were recorded on a UV–vis spectrophotometer (JASCO V-670) in the 200–800 nm range. The electronic environment and chemical composition analysis of $\text{Bi}_7\text{VO}_{13}$ nanoparticles was carried out using X-ray photoelectron spectroscopy with a monochromatic aluminum source, enabling a comprehensive understanding of their properties ($\text{K}\alpha$ line, 1486.6 eV, 14 mA, 9.5 kV, PHI ESCA-5600). The chamber was maintained at 10^{-9} Torr pressure during the measurement. The valance band spectra were obtained using an angle-integrated photoelectron spectroscopy beamline on an INDUS-1 synchrotron radiation source at Raja Ramana Centre for Advanced Technology (RRCAT), Indore, India. In the present measurements, the calibration was done with metallic gold foil, and the data was collected at an incident photon energy of 40 eV.

2.4 Photocatalytic activity

The visible-light-induced photocatalytic activity of $\text{Bi}_7\text{VO}_{13}$ was evaluated for the decolorization of methylene blue (MB) dye. The experimental setup irradiated the sample under visible light at 900 mW/cm^2 . A catalyst mass of 0.1 g was dispersed in a 100 mL solution containing MB at a 10^{-5} M concentration. The experiment was conducted at room temperature. The mixture solution was stirred in the dark for 30 min to achieve adsorption–desorption equilibrium for MB dye. Subsequently, to examine the impact of visible light irradiation, the suspension was collected at 15-minute intervals. The decolorization of MB was assessed by analyzing the absorption spectrum using a UV–vis spectrophotometer.

3 Results

The observed XRD patterns for $\text{Bi}_7\text{VO}_{13}$ nanoparticles were obtained at room temperature along with the Rietveld refinement method using FULLPROF

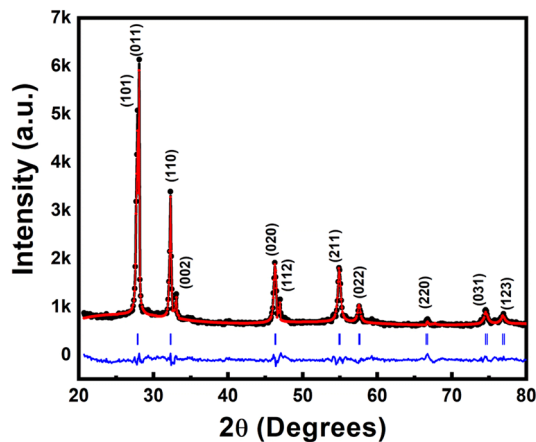


Fig. 1 Powder XRD pattern of $\text{Bi}_7\text{VO}_{13}$ sample

software (pseudo-Voigt function), as shown in Fig. 1. The diffraction peaks were indexed to the crystalline phase with monoclinic symmetry having space group $P 21/n$. No secondary or impurity peaks were observed in the present patterns, which confirms the pure phase of $\text{Bi}_7\text{VO}_{13}$. All the peaks are well-matched with the standard JCPDS files (# 44-0322). The diffraction line observed at $2\theta = 28.06^\circ$ corresponds to the (011) plane characteristic of the monoclinic $\text{Bi}_7\text{VO}_{13}$ compound, and the other nine peaks index with their respective planes confirms the formation of monoclinic structure in the sample. The lattice parameters are $a = 3.992 \text{ \AA}$, $b = 3.936 \text{ \AA}$, $c = 5.431 \text{ \AA}$, and $V = 85.335 \text{ \AA}^3$, which is well matched with an earlier report [23]. The average particle size is $\sim 35 \pm 5 \text{ nm}$, calculated using Debye Scherrer's formula.

The information about the local structure of $\text{Bi}_7\text{VO}_{13}$ nanoparticles was analyzed using Raman spectroscopy, as shown in Fig. 2. The deconvoluted Raman spectra observed six bands at 208, 330, 374, 724, 821 and 915 cm^{-1} . The peak observed at 208 cm^{-1} is associated with the external mode of $\text{Bi}_7\text{VO}_{13}$. The 330 and 374 cm^{-1} peaks are attributed to asymmetric and symmetric deformation modes of V–O bonds in the tetrahedrons. For bismuth vanadate compounds, the distinct V–O stretching frequencies range from 650 to 950 cm^{-1} [14]. The most intense peak was deconvoluted with three peaks. The primary deconvoluted peaks stretching mode observed at 821 cm^{-1} assigned to symmetric $\text{Ag } \nu_s$ (V–O) modes. The weak band at 724 cm^{-1} is assigned to $\text{Ag } \nu_{as}$ (V–O) stretching modes. The deconvoluted peak observed at the tail of the high wavenumber, 915 cm^{-1} , is ascribed to the vibration

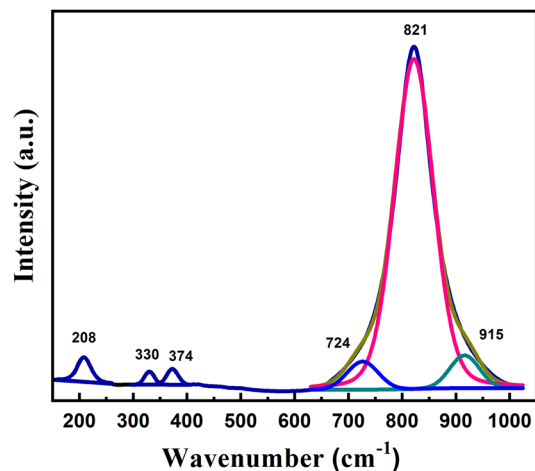
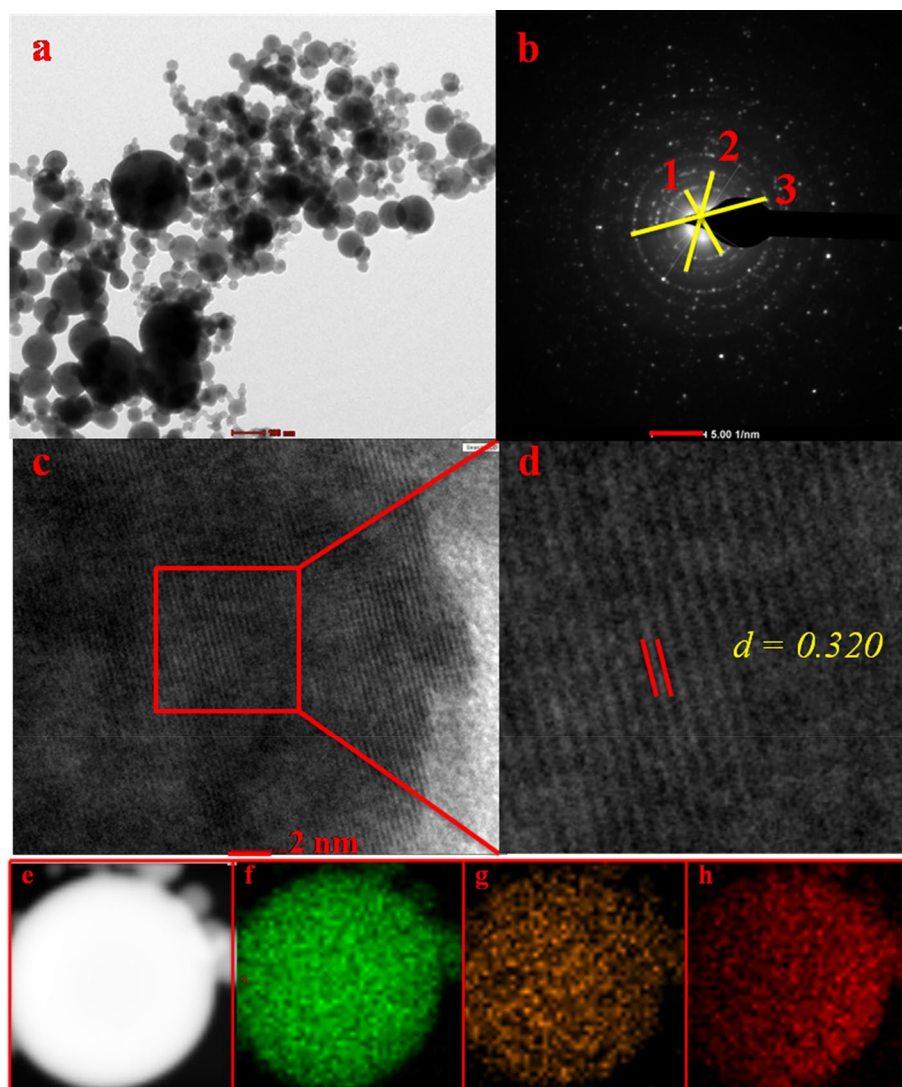


Fig. 2 Raman spectra of $\text{Bi}_7\text{VO}_{13}$ nanoparticles

mode of V–O bonds of distorted trigonal bipyramid [24]. Using the empirical equations ($\nu = 21\,349 \times \exp(-1.917R)$), the V–O bond length by the Raman stretching frequencies is calculated [25, 26]. The V–O stretching mode at 821 cm^{-1} has a bond length of 1.70 \AA , while it has a bond length of 1.65 \AA for 915 cm^{-1} .

To better understand the microstructure of $\text{Bi}_7\text{VO}_{13}$ nanoparticles, transmission electron microscopy (TEM) was performed. Figure 3a typically shows much spherical morphology of the nanoparticles of $\sim 35\text{--}40 \text{ nm}$ in diameter. The size observed from the TEM is analogous to the average particle size calculated using X-ray diffraction. The polycrystalline nature of samples is confirmed by the rings observed in the selected area electron diffraction (SAED) pattern shown in Fig. 3b. The d spacing for the rings observed in the SAED pattern is 0.319 nm , 0.278 nm , and 0.196 nm for rings 1, 2, and 3, respectively. All the d spacing is very well matched with lattice spacing for the planes (011), (110), and (020) of monoclinic $\text{Bi}_7\text{VO}_{13}$ [23]. Figure 3c and d shows the samples' high-resolution TEM image, which reveals sharp and clear lattice fringes, suggesting the nanoparticles are well crystalline. The well-resolved lattice fringes of $d = 0.320 \text{ nm}$ correspond to the (011) plane of monoclinic $\text{Bi}_7\text{VO}_{13}$. Figure 3e–h displays the sample's HAADF-STEM and elemental mapping images. The elemental mapping images of Bi, V, and O were well-defined with sharp contrast, which demonstrates the existence of $\text{Bi}_7\text{VO}_{13}$ nanoparticles. The elemental composition was determined using energy-dispersive X-ray spectroscopy. The calculated average Bi/V ratio was 6.88, close to

Fig. 3 **a** TEM bright images of the $\text{Bi}_7\text{VO}_{13}$ nanoparticles, **b** Selected Area electron Diffraction (SAED) pattern, **c** high-resolution TEM image, **d** Enlarge the view of the selected red square of (c), **e** HAADF – STEM image, **f–h** STEM-EDS elemental mapping of Bi, V, and O respectively



the theoretical stoichiometric value of the chemical formula of $\text{Bi}_7\text{VO}_{13}$.

The pure $\text{Bi}_7\text{VO}_{13}$ nanoparticles exhibit visible light responses in their diffuse reflection spectra, as shown in Fig. 4. This characteristic is beneficial for enhancing photocatalytic activity. The band gap of the nanoparticles is determined by analyzing the absorption edge, which is 2.28 eV. In this system, the conduction bands are formed by the V 3d orbital, whereas the hybrid Bi 6s and O 2p hybrid orbitals form the valence band. The electronic transitions from hybrid orbitals of Bi 6s and O 2p of the valence band (VB) to the V 3d orbitals of the conduction band (CB) give the band gap absorption. The band gap value is significantly narrower than the reported Bi-based compounds such as $\alpha\text{-Bi}_2\text{O}_3$ (2.8 eV) [27] and $\beta\text{-Bi}_2\text{O}_3$ (3.4 eV) [28], Fe doped Bi_2O_3 (2.74

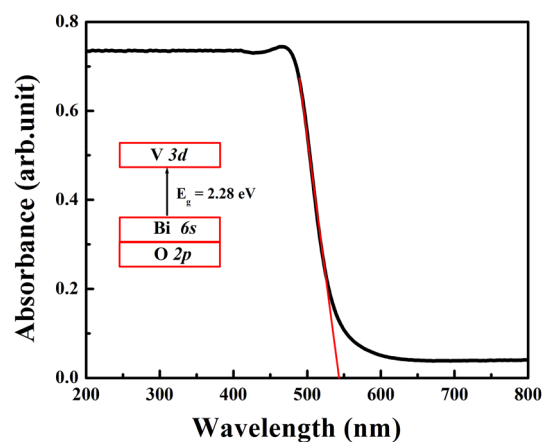


Fig. 4 UV-vis diffuse reflectance spectra of $\text{Bi}_7\text{VO}_{13}$ nanoparticles

eV) [29], tetragonal BiVO_4 [8], Monoclinic BiVO_4 [8], $\alpha\text{-Bi}_2\text{Mo}_3\text{O}_{12}$ (2.92 eV) [30], Bi_2MoO_6 (2.7 eV) [31].

The synthesized material was analyzed by X-ray photoelectron spectroscopy to acquire comprehensive information on the chemical composition and bonding environment of elements. The XPS survey was shown in Fig. 5a in the range of 0–1000 eV, which reveals the presence of Bi, V, and O elements. Due to the spin-orbit splitting effect, the Bi 4f and V 2p observed two peaks in high-resolution spectra of XPS shown in Fig. 5b and c. The binding energy of $\text{Bi}_7\text{VO}_{13}$ for Bi 4f_{7/2} and Bi 4f_{5/2} core level spectra was observed at 158.8 eV and 164.1 eV, respectively, confirming the Bi observed in the 3+ state in the compound. The spin-orbit splitting of Bi 4f peaks is 5.3 eV, which agrees with the reported spin-orbit splitting of the bismuth vanadate system [14].

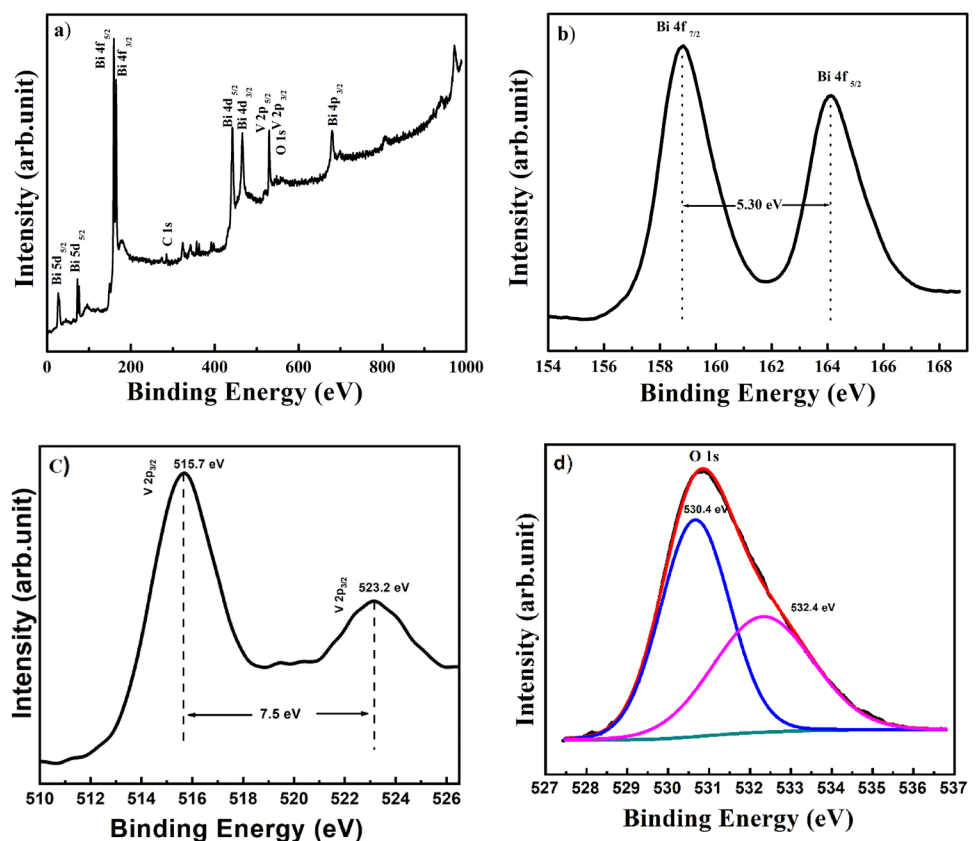
Similarly, Fig. 5c shows that V 2p with 2p_{3/2} and 2p_{1/2} at binding energies of 515.7 eV and 523.2 eV with binding energy separation of 7.5 eV. Moreover, the V 2p spectra confirm the V⁵⁺ state in the $\text{Bi}_7\text{VO}_{13}$ sample. The binding energies and the spin-orbit splitting values are well-matched with the earlier reported values for the vanadate compounds. In Fig. 5d, two peaks at

530.4 eV and 532.4 eV were ascribed to lattice oxygen related to Bi–O or V–O chemical bonding of $\text{Bi}_7\text{VO}_{13}$ and surface adsorbed oxygen species, respectively.

Figure 6 shows the normalized valance band photoemission spectra with an incident photon energy of 40 eV. The valance band spectrum was deconvoluted with four peaks using XPS PEAK41 software. In Fig. 6, peaks are observed at 3.65, 5.25, 7.05, and 8.9 eV, marked as A, B, C, and D, respectively. The peak feature A is associated with unhybridized O 2p with Bi 6s states and O 2p π state. The Bi 6s and O 2p orbitals overlapping in the valance band increases the hole mobility [32]. The peak B observed at 5.25 eV shows the hybridized O sp^2 to V 3d state. The hybridized O sp^2 with Bi 6s state was observed at binding energy 7.05 eV. The peak at higher binding energy, D, is assigned to the Bi 6s state.

We performed X-ray absorption spectroscopy measurements to explore the origin of these optical properties of photocatalytic degradation of bismuth vanadate compounds. Figure 7a and b shows the V L_{3,2}-edge and O K-edge for the $\text{Bi}_7\text{VO}_{13}$ nanoparticles fitted with Voigt functions. The XAS at the V L_{3,2} and O K-edge can provide important information about

Fig. 5 XPS spectra of $\text{Bi}_7\text{VO}_{13}$ nanoparticle **a** Survey scan, **b** Bi 4f, **c** V 2p, **d** O 1s core level spectra



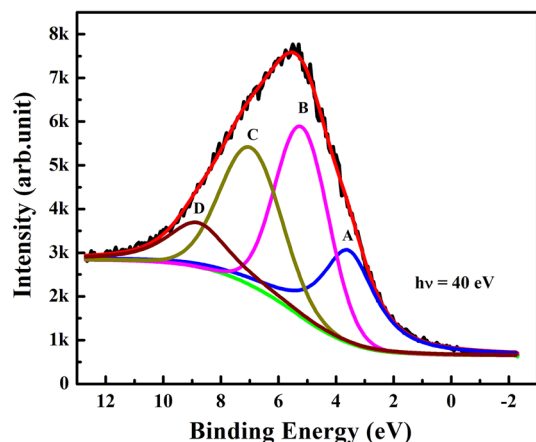


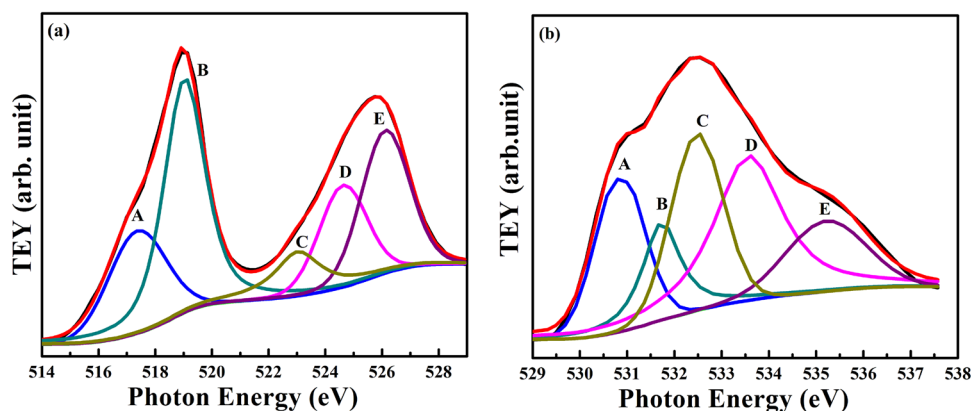
Fig. 6 Valence band spectra for Bi₇VO₁₃ nanoparticles

the unoccupied state within the conduction band and related V valance due to the sensitivity of V $2p_{3/2}$, V $2p_{1/2}$ to V $3d$, O K edge $1s$ to $2p$ dipole transition. Moreover, the spectrum observed broad multiplets because of the separation from the spin-orbit splitting of the V $2p$ core hole, the V L_3 (low energy) peak, and the V L_2 peak (high energy). The conduction band is formed by the hybridization antibonding of V $3d$ states with the antibonding of O sp^2 states. In the upper region of the conduction band, we observed the vital feature of the Bi $6p$ state. The deconvoluted V $L_{3,2}$ edge shows five peaks at 517.2 (A), 519.2 (B), 522.9 (C), 524.6 (D), and 526.1 (E) eV. All these peaks originated from the ligand field splitting of V $3d$ states. Due to the tetrahedral crystal field splitting, the V L_3 edge split into two states, e_g (Peak A) and t_{2g} (Peak B). The peak features A and B reveal the V L_3 edge, showing the transition from occupied $2p_{3/2}$ to the unoccupied $3d$ state of V^{5+} . The separation between e_g and t_{2g} (10Dq value) is 2 eV, which agrees with earlier reports of monoclinic

bismuth vanadate compounds [33]. The V L_2 edge is 6.8 eV above the L_3 edge, indicating a triplet d manifold in Bi₇VO₁₃. The spin-orbit splitting value is slightly higher than the reported value for the monoclinic BiVO₄ structure, which confirmed the marginally different degree of distortion in the V tetrahedral unit than that of the m-BiVO₄ system [33]. The overall XAS spectra confirm the distorted tetrahedral environment of V^{5+} in the monoclinic Bi₇VO₁₃ structure. The XAS at the O K edge can supply helpful additional information on the unoccupied metal states (V $3d$) hybridized with oxygen valence states. The O K edge absorption spectra show the transition from the occupied $1s$ core level to the empty O $2p$ state. The XAS O K-edge spectra deconvoluted into five peaks, A, B, C, D, and E, at binding energies 530.8, 531.6, 532.5, 533.6, and 535.4 eV, respectively. The peak features A, B, and C reveal the O $2p$ to V $3d$ hybridization. These results agree with tetrahedral crystal field splitting of V, e_g , and t_{2g} states. The higher binding energy peaks (Peaks D and E) contribute to Bi $6s$ states.

The photocatalytic activity of Bi₇VO₁₃ nanoparticle was evaluated by degradation of MB under visible light irradiation. Figure 8 shows the full scan UV–visible absorption spectrum to analyze the change observed in the MB absorption (674 nm) spectra under visible light. The photodegraded sample was collected at each 15-minute interval and scanned from the 200–800 nm range. The maximum absorption observed at 674 nm is responsible for the color of the MB dye molecule; in the photodegradation reaction process, it diminishes. The results specify that the absorption peak of MB solution shows a gradual decrease in the absorption peak with increasing irradiation time, and a blue shift of absorption maximum is also observed. This decrease in peak intensity after the visible light

Fig. 7 XAS spectra in the TEY mode for Bi₇VO₁₃ nanoparticles a V $L_{3,2}$ and b O K-edge



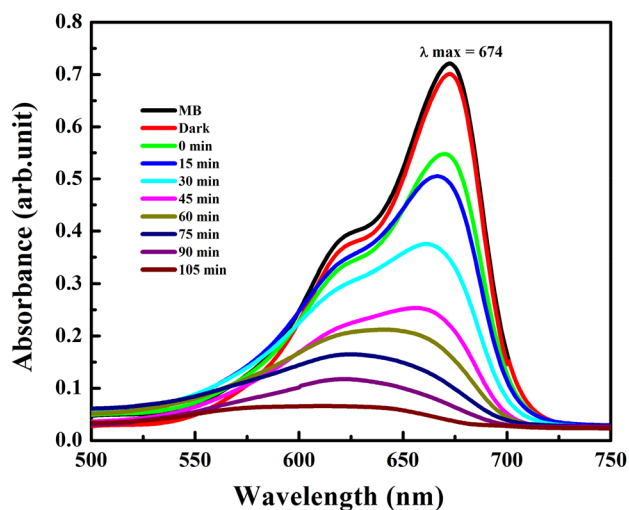


Fig. 8 Absorption spectra of $\text{Bi}_7\text{VO}_{13}$ nanoparticle in methylene blue solution under visible light

irradiation signifies that the solution has been decolorized. No additional peaks are observed during the degradation process, confirming that no reaction intermediates are formed. The blue shift in the absorption spectrum is associated with the hypsochromic effect of MB that occurs by N-demethylation under visible light irradiation [34]. The 90% MB dye was degraded at 105 min time of visible light irradiation.

When exposed to visible light, the $\text{Bi}_7\text{VO}_{13}$ nanoparticle has a remarkable photodegradation rate for MB. Water splitting involves an energetically uphill transformation, characterized by a substantial positive change in Gibbs free energy, measuring 238 kJ/mol. Within the framework of photocatalysis, the semiconductor photocatalyst $\text{Bi}_7\text{VO}_{13}$ is illuminated with energy that matches or surpasses its band gap. When

subjected to light, the semiconductor $\text{Bi}_7\text{VO}_{13}$ absorbs photons, leading to the excitation of electrons from the valence band to the conduction band and creating a hole in the valence band.

The ensuing electron-hole pairs migrate to the surface of the $\text{Bi}_7\text{VO}_{13}$, where they interact with water molecules or hydroxyl ($-\text{OH}$) groups that are adsorbed on the surface. This interaction generates highly reactive species, including superoxide radical anions (O_2^-) and OH^\cdot radicals through redox reactions. These aggressive radicals partake in redox reactions with pollutants adsorbed on the surface, causing a complete degradation of the pollutants. The hole in the valence band is responsible for the direct oxidation of contaminants on the surface, while the electrons present in the conduction band indirectly contribute to the oxidation by generating OH^\cdot radicals. These generated radicals effectively facilitate the breakdown of substantial organic pollutants into less harmful byproducts like water and carbon dioxide.

The detailed mechanism of the photocatalytic reaction is illustrated below. Schematic of the photocatalytic mechanism of $\text{Bi}_7\text{VO}_{13}$ is shown in Fig. 9.

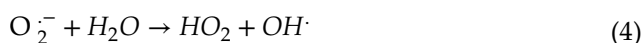
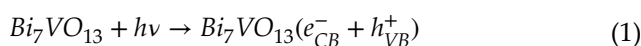
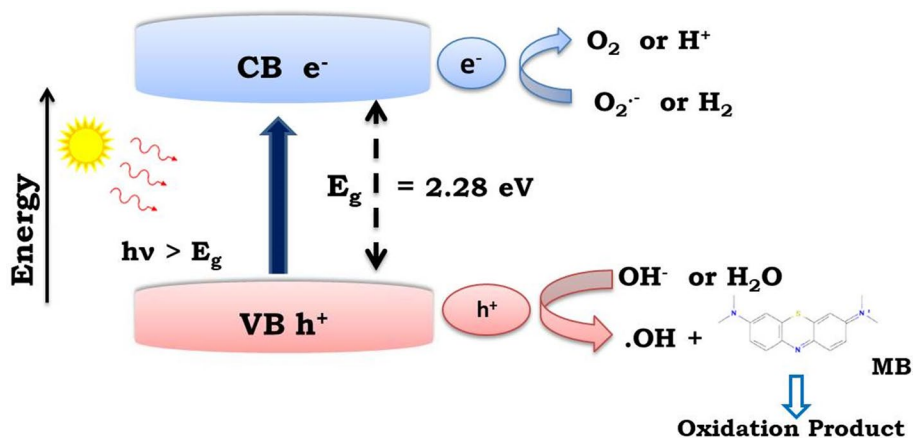


Fig. 9 Schematic of the photocatalytic mechanism of $\text{Bi}_7\text{VO}_{13}$



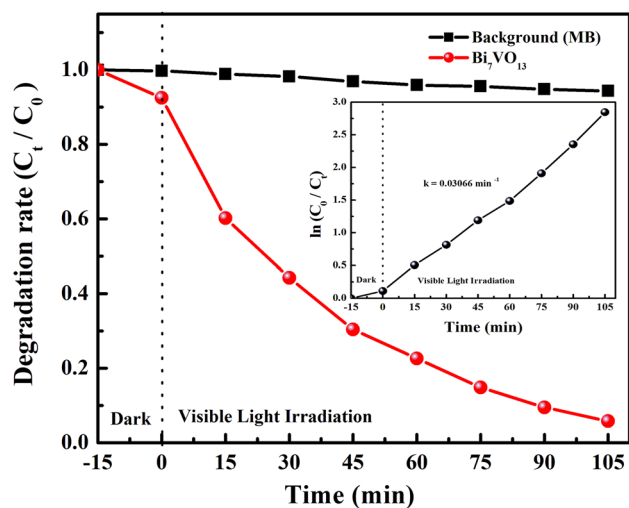
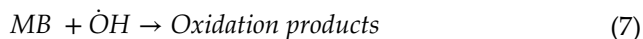


Fig. 10 Photocatalytic degradation rate and the inset shows photodegradation kinetics of MB dye catalyzed by Bi₇VO₁₃ nanoparticles with visible light irradiation



The MB degradation rate versus time is shown in Fig. 10. A blank experiment without a photocatalyst is also performed as a background check under the same condition. The blank experiment observed almost no photocatalytic decolorization of MB after irradiation for 105 min, as indicated by the black line. The blank experiment shows the stability of MB under long-time irradiation. On the contrary, in the presence of Bi₇VO₁₃ nanoparticles, MB shows speedy degradation. Before visible light irradiation, the mixed solution of Bi₇VO₁₃ and MB was stirred in the dark for the adsorption/

desorption equilibrium on the surface of the catalysts. The pseudo-first-order reaction rate equation gives the kinetic rate constant.

The equation is

$$\ln\left(\frac{C_0}{C_t}\right) = kt \tag{8}$$

Where C₀ is the initial concentration,

C_t is the concentration of MB at time t, and

k is the kinetic rate constants.

As the particle size decreases, the surface area increases, efficiently enhancing the photocatalytic activity. The high surface area is an essential parameter for the photocatalytic degradation of organic compounds for adsorption.

The kinetic rate constant k is calculated from the gradient of graph ln(C₀/C_t) as a function of reaction time (t), which exhibits a linear relationship as shown in the inset of Fig. 10 for degradation of MB. The apparent kinetic rate constant (0.03066 min⁻¹) is higher than the earlier reports of Bi-based compounds. The pseudo-first-order kinetic rate constant for some Bi-based compounds shows low kinetic constants such as t-BiVO₄, δ-Bi₂O₃, BiVO₄, the micro ribbon of BiVO₄ (0.0060 min⁻¹) [35], Bi₇VO₁₃ (0.0263 min⁻¹) by Pechini method [23], Bi₁₁VO₁₉ (0.07628 min⁻¹) [14] by thermal plasma method. The photocatalytic activity of oxide semiconductors depends on their crystal structure, band structure, crystallinity, particle size, surface area, and electron-hole recombination rate. The crystal structure is responsible for high photocatalytic activity [36, 37].

According to Pu et al., the (Bi₂O₂)²⁺ layers are dominated by the Bi₇VO₁₃ structure connected by VO₄ layers. In Bi-containing materials (Bi₂O₂)²⁺ layers play a significant role in the photocatalytic activity.

Table 2 Comparative table for Bi-based compound with the kinetic rate constant

Sr. No.	Compound	Synthesis Method	Band Gap	Kinetic Rate Constant	Refs.
1	α- Bi ₂ O ₃	Hydrothermal method	2.72 eV	0.00385 min ⁻¹	[38]
2	t-BiVO ₄	Hydrothermal method	2.92 eV	0.0021 min ⁻¹	[39]
3	m-BiVO ₄	Solvothermal method	2.50 eV	0.0038 min ⁻¹	[40]
4	Bi ₄ V ₂ O ₁₁	Pechini method	2.08 eV	0.0143 min ⁻¹	[41]
5	Bi ₁₁ VO ₁₉	Pechini method	2.23 eV	0.00245 min ⁻¹	[10]
6	Bi ₁₁ VO ₁₉	Thermal plasma method	2.26 eV	0.07628 min ⁻¹	[14]
7	Bi ₇ VO ₁₃	Pechini method	2.13 eV	0.0263 min ⁻¹	[23]
8	Bi ₇ VO ₁₃	Thermal plasma method	2.28 eV	0.03066 min ⁻¹	The present work

The long V-V distance of the polar VO_4 decreases the recombination probability of excitons. Along with structure, the large effective surface area caused by the thermal plasma technique and the suitable electronic band structure are also responsible for increasing the photocatalytic activity. These factors favor enhancing the photocatalytic activity of $\text{Bi}_7\text{VO}_{13}$ nanoparticles [23]. Table 2 summarizes recent studies on different Bi-based compounds showing different photocatalytic applications. We consider some high-temperature phases of Bi-based compounds. Table 2 concludes that, compared to other samples, the sample prepared by the thermal plasma method shows excellent photocatalytic activity.

4 Conclusion

To summarize, we successfully synthesized $\text{Bi}_7\text{VO}_{13}$ nanoparticles using the thermal plasma method for the first time and evaluated their efficiency as a visible light-responsive photocatalyst. The nanoparticles exhibited significantly improved photocatalytic performance. The spherical nanoparticles possess a monoclinic structure with an average particle size of approximately 40 nm, providing a highly effective surface area. Raman spectroscopy validated the structural feature, revealing distortion in the VO_4^{3-} tetrahedron caused by changes in V-O bond lengths. The UV-vis absorption spectrum indicated a wide optical absorption range, corresponding to a narrow band gap of 2.28 eV. TEM analysis examined grain size, crystallinity, and surface morphology. The electronic structure of $\text{Bi}_7\text{VO}_{13}$ nanoparticles was comprehensively investigated using X-ray spectroscopy techniques, such as XPS, VBS, and XAS. Our results confirmed that the valence band maximum primarily consisted of Bi 6s – O 2p states, while the conduction band minimum comprised V 3d states with minor contributions from O 2p and Bi 6p states. The local structural distortion within the valence band influenced the overlap between Bi 6s and O 2p states, leading to increased hole mobility. The photocatalytic efficiency of $\text{Bi}_7\text{VO}_{13}$ nanoparticles was assessed by determining the degradation of MB dye under visible light. Our kinetic study demonstrated that the photodegradation reactions follow pseudo-first-order kinetics, with a higher rate constant ($k = 0.03066 \text{ min}^{-1}$) than previous reports. These nanoparticles exhibited excellent photocatalytic

activity. The thermal plasma synthesis technique, with its highly effective surface area, local structure control, crystallinity, and suitable band alignment, significantly influenced the photocatalytic performance in the degradation of MB dye under visible light irradiation.

Acknowledgements

The authors thank UGC-BSR, Delhi, for the financial assistance to conduct this research. The authors also thank Mr. Avinash Wadiker for his help in XPS and VBS measurements at the AIPES beam line on INDUS-1.

Author contributions

SSK and SAR designed experiments and characterized samples. SSK and SAR synthesized the sample and analyzed the data. SSK carried out XPS, VBS, and XAS measurements and analyzed data with RJC and DP. The manuscript was written through the contribution of all authors. All authors have approved the final version of the manuscript.

Funding

Dr. Kekade S. S. reports that UGC-BSR, Delhi provided financial support.

Declarations

Competing interests The authors have no relevant financial or non-financial interests to disclose.

Supplementary information The online version contains supplementary material available at <https://doi.org/10.1007/s10854-023-11732-9>.

References

1. M. Suresh, A. Sivasamy, J. Environ. Chem. Eng. **6**, 3745–3756 (2018)
2. S. Zheng, W. Jiang, Y. Cai, D.D. Dionysiou, K.E. O’Shea, Catal. Today **224**, 83–88 (2014)

3. Z. Hao, L. Xu, B. Wei, L. Fan, Y. Liu, M. Zhanga, H. Gao, *RSC Adv.* **5**, 12346–12353 (2015)
4. M.Y. Wang, J. Iocozia, L. Sun, C.J. Lin, Z.Q. Lin, *Energy Environ. Sci.* **7**, 2182–2202 (2014)
5. A. Kusior, K. Michalec, P. Jelen, M. Radecka, *Appl. Surf. Sci.* **476**, 342–352 (2019)
6. V. Dutta, S. Sharma, P. Raizada, V.K. Thakur, A. Aslam, P. Khan, V. Saini, A.M. Asiri, P. Singh, *J. Environ. Chem. Eng.* **9**, 105018 (2021)
7. A.P. Reverberi, P.S. Varbanov, M. Vocciante, B. Fabiano, *Front Chem. Sci. Eng.* **12**, 878–892 (2018)
8. S. Tokunga, H. Kato, A. Kudo, *Chem. Mater.* **13**, 4624–4628 (2001)
9. Y.H.B. Liao, J.X. Wang, J.S. Lin, W.H. Wan, C.C. Chen, *Catal. Today.* **174**, 148–159 (2011)
10. Y. Lu, L. Chen, Y. Huang, H. Cheng, S. Kim, H. Seo, *J. Alloys Compd.* **640**, 226–232 (2015)
11. B. Scola Rodrigues, C.M. Branco, P. Corio, J.S. Souza, *Cryst. Growth Des.* **20**, 3673–3685 (2020)
12. G.S. Kamble, T.S. Natarajan, S.S. Patil, M. Thomas, R.K. Chougale, P.S. Sanadi, U.S. Sidharth, Y.C. Ling, *Nanomaterials* **13**, 1528 (2023)
13. A. Kudo, K. Omori, H. Katol, *J. Am. Chem. Soc.* **121**, 11459–11467 (1999)
14. S.S. Kekade, P.V. Gaikwad, S.A. Raut, R.J. Choudhary, V.L. Mathe, D.M. Phase, A.L. Kshirsagar, S.I. Patil, *ACS Omega* **3**, 5853–5864 (2018)
15. S. Gong, Q.F. Han, J.W. Zhu, X. Wand, J.D. Lu, *Mater. Res Bull.* **76**, 222–228 (2016)
16. J.L. Hu, W.J. Fan, W.Q. Ye, C.J. Huang, X. Qiu, *Appl. Catal. B* **158**, 182–189 (2014)
17. M.X. Du, Y. Du, Y.B. Feng, K. Yang, X.J. Lv, N. Jiang, Y. Liu, *Carbohydr. Polym.* **195**, 393–400 (2018)
18. H.B. Li, Z.J. Yang, J.N. Zhang, Y.C. Huang, H.B. Ji, Y.X. Tong, *Appl. Surf. Sci.* **423**, 1188–1197 (2017)
19. C.Y. Wang, X. Zhang, X.N. Song, W.K. Wang, H.Q. Yu, *ACS Appl. Mater. Interfaces* **8**, 5320–5326 (2016)
20. S. Jonjana, A. Phuruangrat, T. Thongtem, S. Thongtem, *Mater. Lett.* **172**, 11–14 (2016)
21. D.P. Macwan, C. Balasubramanian, P.N. Dave, S. Chaturvedi, *J. Saudi Chem. Soc.* **18**, 234–244 (2014)
22. S.A. Raut, N.S. Kanhe, S.V. Bhoraskar, A.K. Das, V.L. Mathe, *J. Appl. Phys.* **116**, 163913 (1–6) (2014)
23. Y. Pu, Y. Li, Y. Huang, S. Kim, P. Cai, H.J. Seo, *Mater. Lett.* **141**, 73–75 (2015)
24. O. Attos, *J. Non-Cryst. Solids* **210**, 163–170 (1997)
25. I.D. Brown, K.K. Wu, *Acta Crystallogr. B* **32**, 1957–1959 (1976)
26. F.D. Hardcastle, I.E. Wachs, *Solid State Ion.* **45**, 201–213 (1991)
27. Z. Ai, Y. Huang, S. Lee, L. Zhang, *J. Alloys Compd.* **509**, 2044–2049 (2011)
28. M. Schlesinger, M. Weber, S. Schulze, M. Hietschold, M. Mehring, *Chem. Open* **2**, 146–155 (2013)
29. W. Xiaohong, Q. Wei, L. Li, G. Yun, X. Zhaoyang, *Catal. Commun.* **10**, 600–604 (2009)
30. H. Hua Li, K.W. Li, H. Wang, *Mater. Chem. Phys.* **116**, 134–142 (2009)
31. M. Zhang, C. Shao, P. Zhang, C. Su, X. Zhang, P. Liang, Y. Sun, Y. Liu, *J. Hazard. Mater.* **225**, 155–163 (2012)
32. Y. Wan, S. Wang, W. Luo, L. Zhao, *Int. J. Photoenergy* **1155**, 1–7 (2012)
33. A. Chaudhuri, L. Mandal, X. Chi, M. Yang, M.C. Scott, M. Motapothula, X.J. Yu, P. Yang, Y. Shao-Horn, T. Venkatesan, A.T.S. Wee, A. Rusydi, *Phys. Rev. B* **97**, 195150 (1–8) (2018)
34. T. Zhang, T.K. Oyama, S. Horikoshi, H. Hidaka, J. Zhao, N. Serpone, *Sol. Energy Mater. Sol Cells* **73**, 287–303 (2002)
35. G. Liu, S. Liu, Q. Lu, H. Sun, F. Xu, G. Zhao, *J. Sol-Gel Sci. Technol.* **70**, 24–32 (2014)
36. G. Liu, S. Li, Y. Lu, J. Zhang, Z. Feng, C. Li, *J. Alloys Compd.* **689**, 787–799 (2016)
37. N.S. Azhar, M.F.M. Taib, O.H. Hassan, M.Z.A. Yahya, A.M.M. Ali, *Mater. Res. Express* **4**(034002), 1–7 (2016)
38. Z. Ai, Y. Huang, S. Lee, L. Zhanga, *J. Alloys Compd.* **509**, 2044–2049 (2011)
39. A. Zhang, J. Zhang, N. Cui, X. Tie, Y. An, L. Li, *J. Mol. Catal. A: Chem.* **304**, 28–32 (2009)
40. G.S. Kamble, Y.C. Ling, *Sci. Rep.* **10**, 12993 (2020)
41. Y. Lu, Y. Pu, J. Wang, C. Qin, C. Chen, H.J. Seo, *Appl. Surf. Sci.* **347**, 719–726 (2015)

Publisher's note Springer Nature remains neutral with regard to jurisdictional claims in published maps and institutional affiliations.

Springer Nature or its licensor (e.g. a society or other partner) holds exclusive rights to this article under a publishing agreement with the author(s) or other rightsholder(s); author self-archiving of the accepted manuscript version of this article is solely governed by the terms of such publishing agreement and applicable law.